Halide Perovskite Solar Cells Using Monocrystalline TiO_2 Nanorod Arrays as Electron Transport Layers: Impact of Morphology

Ujwal Kumar Thakur,[1] Abdelrahman M. Askar,[1] Ryan Kisslinger,[1] Benjamin D. Wiltshire,[1] Piyush Kar[1] and Karthik Shankar[1,2]

[1]*Department of Electrical and Computer Engineering, University of Alberta, 9211-116 St, Edmonton, Alberta, T6G 1H9, Canada*

[2]*NRC National Institute for Nanotechnology, 11421 Saskatchewan Dr NW, Edmonton, AB T6G 2M9, Canada*

ABSTRACT

This is the first report of a 17.6 % champion efficiency solar cell architecture comprising monocrystalline TiO_2 nanorods (TNRs) coupled with perovskite, and formed using facile solution processing without non-routine surface conditioning. Vertically oriented TNR ensembles are desirable as electron transporting layers (ETLs) in halide perovskite solar cells (HPSCs) because of potential advantages such as vectorial electron percolation pathways to balance the longer hole diffusion lengths in certain halide perovskite semiconductors, ease of incorporating nanophotonic enhancements, and optimization between a high contact surface area for charge transfer (good) vs. high interfacial recombination (bad). These advantages arise from the tunable morphology of hydrothermally grown rutile TNRs, which is a strong function of the conditions of growth. Fluorescence lifetime imaging microscopy (FLIM) of the HPSCs demonstrated a stronger quenching of the perovskite photoluminescence when using TNRs as compared to mesoporous TiO_2 thin films of similar thickness and planar TiO_2 ETLs. Such a high charge separation efficiency in TNR-based HPSCs is due the large interfacial contact area between the ETL and perovskite along with the ease of pore filling of the TNR ETL by the perovskite. At the same time, the low surface free electron density in hydrothermally grown

single crystal rutile TNRs suppressed interfacial recombination between the electrons in the TNR ETL and photogenerated holes in the perovskite. The optimal ETL morphology in this study was found to consist of an array of TNRs ~ 300 nm in length and ~ 40 nm in width. This work highlights the potential of TNR ETLs to achieve high performance solution-processed HPSCs.

1. Introduction

Organometal trihalide perovskite materials with the composition ABX_3 [A=Cs^+, $CH_3NH_3^+$ (MA), or $NH{=}CHNH_3^+$ (FA); B = Pb or Sn; X= Br or I] are the focus of intense worldwide research interest for use as light-absorbing materials in photovoltaic cells because of their outstanding optoelectronic properties such as a direct optical bandgap, broadband light absorption, ambipolar transport, and long carrier diffusion lengths. In the last decade, a remarkable enhancement in the PCE of perovskite solar cells has been demonstrated. Miyasaka *et al* reported the first perovskite solar cell in 2006 [1] with a PCE of 2.2 %, which they improved to 3.8 % in 2009 [2]. Intensive research into the development of HPSCs is now in progress which has led to a current highest certified PCE of 22.1 % [3]. In general, certain members of the organometal trihalide perovskite semiconductor family including $MAPbI_3$ and $FAPbI_3$ have a lower effective electron diffusion length compared to the effective hole diffusion length in solution cast thin films [4, 5], an issue which one-dimensional electron transport layers (1D-ETLs) can assist with, because of which nanostructured ETLs offer the potential to enhance the performance of HPSCs [4, 6, 7]. The nanostructured ETL not only improves electron transport but also provides a mechanical support and scaffold for the perovskite absorber layer in solar cells. Nanostructured ETLs could also be used to reduce thermodynamic losses related to photons [8, 9] through incorporation of a number of nanophotonic effects such as photonic bandgap crystals [10-13], resonant and non-resonant Mie scatterers [14, 15], whispering gallery modes [16] and waveguide modes [17]. Transparent

semiconducting metal oxides such as TiO_2, SnO_2, ZnO, $SrTiO_3$ and WO_3 are the most commonly used ETL materials which ensure efficient contact with the perovskite active layer and selectively transfer photogenerated electrons to the underlying electrode while also blocking holes [18-22]. Mesoporous TiO_2 is the most common ETL used for perovskite solar cells. The mesoporous architecture is comprised of a large number of *ca.* 20 nm-sized nanoparticles with many grain boundaries; this restricts the flow of electrons, resulting in poor charge transfer. Furthermore, the mesoporous architecture does not provide a unified path to photogenerated electron flow which leads to a random walk of electrons through the ETL [23, 24]. Such a random walk-type transport increases the length of the path electrons must travel to the collecting electrode and increases the probability of recombination. To overcome problems associated with the mesoscopic structure, a tremendous effort is being devoted towards the application of 1D-ETLs in HPSCs. 1D-ETLs provide a direct path for photogenerated electron transport and have a large internal surface area, leading to fast charge transport, efficient charge separation and a superior charge collection efficiency. 1D-ETLs also provide better pore filling of the perovskite absorber than the nanoparticulate structure in mesoscopic TiO_2 thin films because of their open pore structure [25-27]. TiO_2, ZnO, WO_3, and CdS nanorods and nanotubes have been tested as ETLs for perovskite solar cells, but only TiO_2 nanorods (TNRs) have consistently produced HPSCs with PCEs above 15 % [28-31]. Several works on the application of TNRs as ETLs have been documented. Qui *et al* reported TNRs sensitized using an extra thin layer of $CH_3NH_3PbBr_3$ having a PCE of 4.87 % [32]. Park *et al* compared the photovoltaic performance of long (> 1 μm) and short (< 1 μm) TNRs, and found that the shorter nanorods provided better infiltration of perovskite. By using 560 nm long nanorods, they achieved a PCE of about 9.4 % [27]. Jiang *et al* tried to further optimize the length of nanowires for high

performance HPSCs; they found that increasing the length of nanowires to 900 nm helps to improve PCE by enhancing short-circuit current density while increasing the length to 1.2 µm drastically reduces the short circuit current and open circuit voltage [33]. Recently, Li *et al* [30] reported perovskite solar cells with a PCE of 18.2 %. They tuned the morphology of titania nanorods by using different organic acids in the growth solution of nanorods and used a UV-ozone treatment to improve the TNR/perovskite interface [30]. Unlike the use of organic acids or plasma treatment or ALD coatings on the surface, the only surface treatment employed by us was the well-established $TiCl_4$ treatment, which is considered routine for nanostructured TiO_2 [34-36]. A major criticism of several of the aforementioned reports is the superficial nature of the discussion related to device performance. Herein, we present an in-depth discussion of the electrical behavior of HPSCs based on TNR ETLs, which is extremely necessary in order to understand the sources of both underperformance and outperformance in various device parameters so as to enable the achievement of even higher efficiencies close to the S-Q limit [37]. We performed a detailed study of the effect of the nanorods on the optical properties of the resulting HPSCs. We demonstrated the effect of morphology on charge separation and recombination at the perovskite/TNR interface. We optimized the morphology of hydrothermally grown rutile nanorods to produce perovskite solar cells with a champion PCE of 17.6 %.

2. Experimental

2.1 Synthesis of TiO_2 nanorod arrays

Titanium (IV) *n*-butoxide, Titanium (IV) isopropoxide, acetonitrile**,** lead iodide and lead bromide was purchased from Acros Organics. Acetic acid, HCl, formamidinium iodide, 4-tert-butylpyridine, lithium bis(trifluoromethanesulfonyl)-imide and spiro-OMeTAD were purchased from Sigma-Aldrich. Methylammonium bromide was obtained from Dyesol. Chlorobenzene,

Titanium (IV) Chloride, dimethylformamide (DMF) and dimethylsulfoxide (DMSO) were purchased from Fisher Scientific. Chemicals were used as received without any further purification. Fluorine-doped tin oxide (FTO) coated glass slides (Hartford Tec Glass Company) were used as substrates and were first cleaned by sonicating in acetone, methanol and deionized water for 10 minutes each. A thin compact layer of TiO_2 was deposited on the cleaned FTO:glass substrate (Fig. 1a). The precursor solution for the deposition of compact TiO_2 was prepared by a method described elsewhere; in brief, 369 µl of titanium (IV) isopropoxide and 70 µl of 1 M HCl were separately diluted in 2.53 ml of isopropanol. Diluted HCl was added drop by drop into the diluted titanium (IV) isopropoxide solution under stirring. After overnight stirring of the mixed solution, it was filtered using a 0.2 µm filter and deposited over cleaned FTO:glass substrates by spin casting at 3000 RPM for 30 seconds, followed by calcination at 450 ºC for 30 min [38-40]. The TiO_2 nanorod array was grown on the FTO/TiO_2 substrate by a simple hydrothermal method. 2.5 ml of HCl (37%) and 2.5 ml of glacial acetic acid were mixed with 5 ml of DI water in ambient conditions. The mixture was processed in a Teflon-lined stainless steel autoclave after adding the proper amount of titanium (IV) *n*-butoxide (TBO) into it. The substrate was placed in the autoclave at an angle such that the FTO/TiO_2 side faced downwards. The autoclave was then sealed and hydrothermal growth was conducted at 200º C for 30 min in a laboratory oven (Fig. 1b). Subsequent to nanorod growth, the autoclave was cooled to room temperature in ambient air; the resulting transparent nanorod array (Fig. 1c) was rinsed with DI water for 2 min and dried in a stream of flowing nitrogen. The TNR array was then treated with 40 mM of $TiCl_4$ at 70 ºC for 30 minutes and annealed at 500 ºC for 30 mins. Mesoporous TiO_2 ETLs were deposited on FTO/TiO_2 by spin casting followed by calcination at 500 ºC for 30 min.

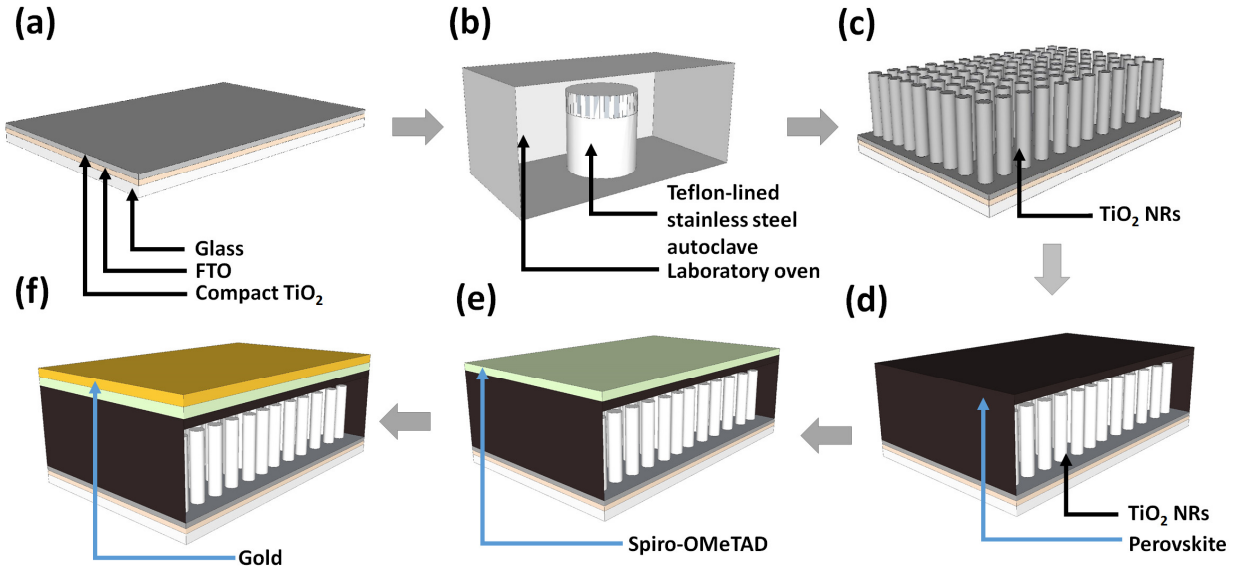

Fig. 1. Schematic illustration of perovskite solar cell fabrication based on TiO_2 nanorods (a) Compact TiO_2 layer deposited over clean FTO:glass substrate (b) Hydrothermal growth of TNRs on FTO:glass substrates in laboratory gravity convection oven at 200°C for 1 hr (c) Grown rutile TNR array and (d, e, and f) Perovskite active layer, spiro-OMeTAD and gold electrode deposited over $TiCl_4$-treated rutile nanorods.

2.2 Characterization

The morphologies of the TNRs and the TNR-perovskite solar cells were imaged using a Hitachi S4800 cold field emission scanning electron microscope (FESEM) using an accelerating voltage of 5 kV and a beam current of 20 μA. UV-Vis-NIR spectroscopy was performed using a Perkin Elmer Lambda-1050 spectrophotometer equipped with a 100 mm integrating sphere accessory. Steady state photoluminescence (PL) spectra were collected using a Varian Cary Eclipse spectrofluorometer. Fluorescence lifetime imaging (FLIM) was performed using a Zeiss LSM 510 NLO multi-photon microscope equipped with a Ti:sapphire laser and a FLIM module consisting of a Hamamatsu RS-39 multi-channel plate detector, a filter wheel and a Becker Hickl SPC730 board for photon counting. The fluorescence decay curve was constructed by synchronizing information from a photodiode and from the laser pulses. Solid state impedance

spectroscopy (SSIS) was performed in a two electrode configuration using a CHI-600E potentiostat.

2.3 Device fabrication and testing

Devices were fabricated on FTO coated glass substrates (henceforth referred to as FTO:glass) having a sheet resistance of 8 Ω/□. To prevent shunting upon contact with measurement pins, the FTO:glass substrates were patterned using 35 % HCl and Zn powder. The perovskite precursor solution consisted of 1 M formamidinium iodide (FAI), 1.1 M PbI_2, 0.2 M methylammonium bromide (MABr) and 0.22 M $PbBr_2$ in a 4:1 mixture of DMF and DMSO. The precursor solution was stirred for 2 hours at 70 ºC before being deposited on the TNRs. The perovskite solution was deposited on nanorods in a two-step procedure: first at 1000 rpm for 10 sec and then at 4000 rpm for 20 sec. 100 µl of chlorobenzene was dropped on the spinning substrate at the 15^{th} second of the second step for rapid crystallization. Substrates ware then annealed at 100 ºC for 30 min (Fig. 1d). A hole transporting layer was deposited by spin-casting a solution containing 35 mg of Spiro-OMeTAD mixed with 1 ml of chlorobenzene and additives, namely 4.4 mg of lithium bis(trifluoromethanesulfonyl)-imide, 14 µl of 4-tert-butylpyridine and 17.5 µl of acetonitrile; this resulted in a hole transporting layer roughly 200 nm thick (Fig. 1e). A 70-nm thick layer of gold was then thermally evaporated to complete the devices (Fig. 1f). The current-voltage characteristics of the samples were measured using a Keithley 4200 semiconductor parameter analyzer. For solar cell testing, one sun AM1.5 illumination from a collimated Class A solar simulator (Newport Instruments) was used. Incident photon-to-electron conversion efficiency (IPCE, also known as external quantum yield or EQE) was measured using a home-built set-up consisting of a Xe arc lamp, chopper, filter-wheel, computer-controlled monochromator, calibrated silicon photodetector and optical power meter.

3. Results and Discussion

The concentration of the Ti precursor used in the hydrothermal growth process plays a crucial role in determining the morphology of grown nanorods. Fig. 2 shows cross-sectional and top-view FESEM images of rutile TNR arrays grown with different concentrations of TBO in the acid digestion vessel. For a constant growth temperature and duration - the length, width and packing density of square cross-sectioned nanorods increase with increasing concentration of TBO in the precursor solution. The dimensions of the nanorods were determined to be ~ 100 nm long and ~ 20 nm wide for 400 µl of TBO (A-type), ~ 300 nm long and ~ 40 nm wide for 600 µl of TBO (B-type), ~ 650 nm long and ~ 80 nm wide for 800 µl of TBO (C-type) as shown in Fig. 2a-f, and ~ 800 nm long and ~ 150 nm wide for 1000 µl of TBO (D-type). The length and packing density of the nanorods are important parameters which decide the photovoltaic performance of the final HPSCs. Short nanorods with a large inter-wire spacing between nanorods do not provide a sufficient number and areal density of heterojunctions for charge separation because of a low roughness factor and a low surface area. A high loading of the perovskite absorber and an interwire spacing well below half twice the electron diffusion length are essential to ensure maximum transfer of photogenerated electrons from the perovskite active layer to the rutile nanorods. On the other hand, a very long and densely packed TNR array suffers from poor infiltration of perovskite compared to relatively shorter nanorods with larger interspacing [27, 41-43] and also increases the probability of recombination of electrons transiting through the TNRs toward the FTO electrode with holes transiting in the perovskite toward the Au electrode. Therefore the morphology of nanorods must be optimized so that it can provide a large surface area with sufficient infiltration of the active layer.

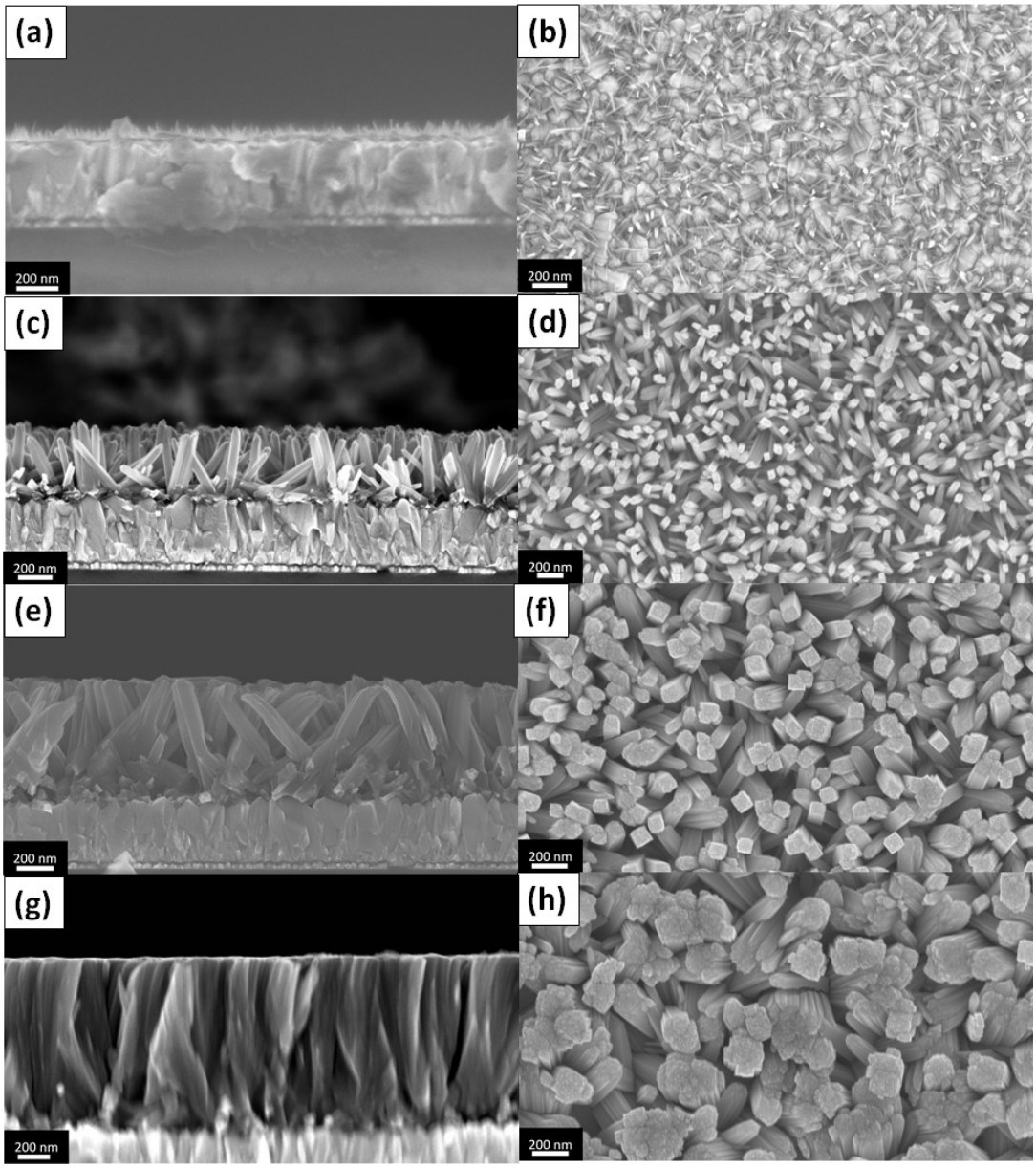

Fig. 2. Cross-sectional and top-view SEM images of A-type, B-type, C-type and D-type TiO_2 nanorod arrays grown on FTO substrate at 200°C for 1 h using (a, b) 400 µl (c, d) 600 µl (e, f) 800 µl and (g, h) 1000 µl of titanium (IV) *n*-butoxide in the hydrothermal precursor solution respectively.

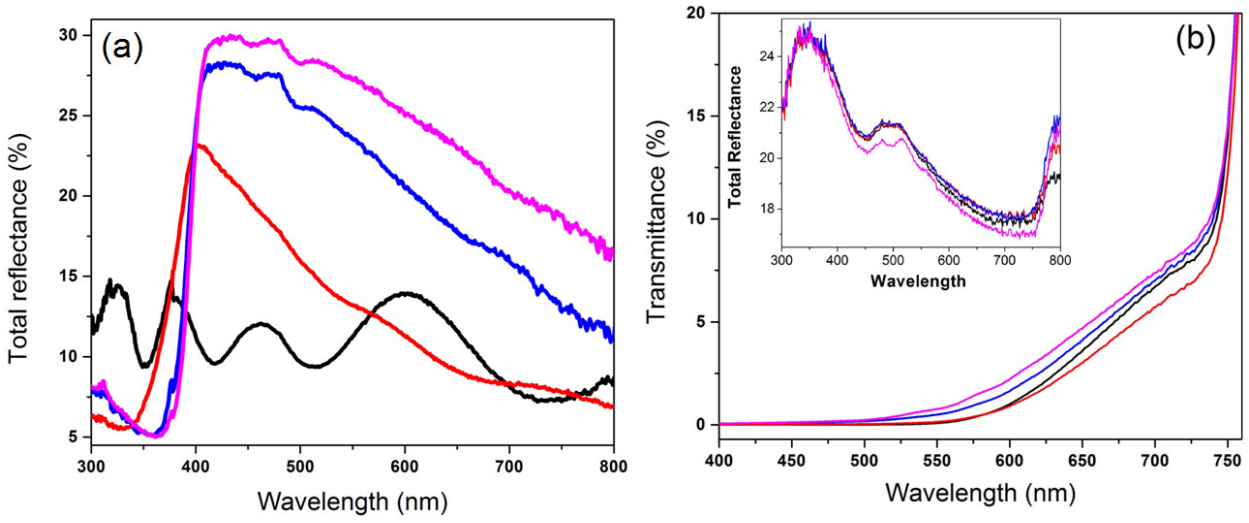

Fig. 3 (a) Total reflectance (including both specular and diffuse reflectance) spectra of TiO_2 nanorods made with different concentrations of TBO; light is incident directly on the TNRs (b) Total transmittance (including both directly transmission and forward scattering) spectra of TiO_2 nanorod-perovskite blends with the inset showing the total reflectance of the same blends; light is incident through the FTO:glass substrate. Black, red, blue and purple colors represent A-type, B-type, C-type and D-type TiO_2 nanorods with lengths of 100 nm, 300 nm, 650 nm and 1000 nm respectively formed by adding 400 µl, 600 µl, 800 µl and 1000 µl of titanium (IV) *n*-butoxide into hydrothermal precursor solution respectively.

The morphology of nanorods also plays a considerable role in its light scattering behavior which has a significant effect on the light harvesting efficiency of a solar cell. In dye sensitized solar cells (DSCs), the correct design and incorporation of Mie scatterers has been used to improve the light harvesting efficiency of near band-edge photons (~ 700-750 nm) by increasing the optical path lengths of red photons inside the nanostructures [44-46]. However, DSCs consist of a 10-12 µm thick dye-coated nanostructured TiO_2 film coupled to a 3-5 µm thick scattering layer which allows backscattered light from the rear of the solar cell to be efficiently absorbed in the rest of the dye-coated film. On the other hand, the thickness of the active layer in HPSCs is typically much smaller than 1 µm, due to which the conditions of scattering are different.

Furthermore, in the 'inverted' solar cell geometry used in this study (see Fig. 1), the TNRs are the scatterers and are placed at the front of the solar cell rather than at the rear, due to which backscattering can actually decrease light harvesting by coupling light out of the solar cell and forward scattering needs to be matched to the absorption of succeeding layers to improve light harvesting. The light scattering properties of TNR arrays grown with different concentrations of TBO were studied and are depicted in Fig. 3. For A-type nanorods, Mie scattering is not significant and the reflectance spectrum is dominated by interference fringes (black curve in Fig. 3a). The peak in the total reflectance spectrum plateaus and redshifts as the characteristic dimension increases [15, 47-49], a behavior also observed in Fig. 3 for TNRs of larger widths formed using increasing concentrations of TBO. Several different TiO_2 nanostructures with dimensions in the range 50–300 nm, are reported to exhibit maximum back scattering at ~ 400 nm [15, 47-49] similar to that observed in Fig. 3a. The reflectance spectra of the perovskite-filled TNRs are shown in the inset of Fig. 3b whose most obvious feature is the nearly identical values of total reflectance exhibited by each of the four nanorod morphologies investigated in this study. Since Mie scattering is a strong function of the dimensions of the nanostructures, the lack of morphology dependence is indicative of the dominance of specular reflection rather than diffuse reflection for the nanorod morphologies studied. Interfaces with sharp changes in the refractive index give rise to strong specular reflection. There are three such interfaces for the samples studied here: (i) The air-glass interface (ii) the glass-FTO interface and (iii) the FTO-blend film interface. Over the UV-Vis-NIR spectra range, the refractive index of glass is ~ 1.5 and that of FTO is ~ 2.0. As far as the TNR-perovskite blend is concerned, both the rutile phase of TiO_2 and the perovskite have refractive indices of ~ 2.6 over the wavelength range of interest. Therefore, strong reflections are expected from each of the aforementioned interfaces. Two

prominent peaks are seen in the reflection spectra in the inset of Fig. 3b, one at ~ 350 nm and the other at ~ 500 nm. Rutile-phase TiO_2 exhibits a maximum refractive index of 3.95 at ~ 330 nm and Tec-8 FTO:glass substrates such as those used in this study, are known to have a maximum in their reflection spectra at ~ 350 nm [50], and the peak in the ultraviolet corresponding to these maxima is clearly seen in the inset of Fig. 3b. The reflectance peak at ~ 500 nm is due to the perovskite exhibiting a maximum refractive index of 2.79 at ~ 500 nm [51]. Fig. 3b shows that B-type TNRs blended with perovskite (red curve in Fig. 3b) have the lowest total transmittance indicating it to be the morphology resulting in the most efficient harvesting of light. Significant optical reflectance losses at the front end of the solar cell due to the sharp changes in refractive index at the air-glass, glass-FTO and FTO-TNR+perovskite interfaces suggest the need for texturing of the interfaces while light trapping structures such as multilayer TNRs with different nanorod widths at the rear end of the solar cell can improve the utilization of photons at the band edge.

Table 1. Photovoltaic performance of HPSCs under AM 1.5 simulated light as a function of the morphology of TiO_2 nanorods used as the ETL.

Mophology		V_{oc} **(V)**	J_{sc} **(mA/cm^2)**	**FF**	**PCE (%)**
A-type	Average	1.01±0.02	21.86±1.07	0.64±0.02	14.08±0.70
	Champion	1.01	21.19	0.67	14.3
B-type	Average	0.99±0.03	23.17±0.32	0.72±0.03	16.57±1.04
	Champion	1.00	23.08	0.76	17.6
C-type	Average	0.91±0.04	20.85±1.15	0.62±0.02	11.74±0.47
	Champion	0.96	20.72	0.62	12.26

The photovoltaic performance of perovskite solar cells fabricated on different types of TNR arrays are summarized in Table 1 and Fig. S1. The photovoltaic performance of champion cells

based on all the three nanorod morphologies is shown in Fig. 3 (a). One sun illumination of the solar cell based on A-type nanorod arrays yielded an average PCE of 14.08 ± 0.70%, resulting from open circuit voltage (V_{oc}) of 1.01 ± 0.02 V, photocurrent density (J_{sc}) of 21.86 ± 1.07 mA cm^{-2} and fill factor (FF) of 0.64 ± 0.02. The solar cell based on the B-type TNR arrays showed improvement in J_{sc} and FF with corresponding improvement in PCE to 16.57 ± 1.04 %. Upon further increasing the length of the nanorods to ~ 650 nm and the width to ~ 80 nm (C-type NRs), a significant decrease in V_{oc}, J_{sc}, and FF was observed resulting in the corresponding decrease in PCE to 11.74 ± 0.47 %. The maximum J_{sc} being obtained for B-type TNR arrays correlates well with this morphology harvesting light most efficiently as shown in Fig. 3 and Fig. 4d, and explained previously. J_{sc} is proportional to IPCE which is a product of light harvesting efficiency (η_{lh}), charge separation efficiency (η_{cs}) and the charge collection efficiency (η_{cc}). Fig. 4c show that for all three nanorod morphologies whose IPCE action spectra are plotted, the lowest external quantum yields occur for at ~ 400 nm (other than in the near band edge spectral region). A partial explanation of this phenomenon is the high specular reflection observed for blue and ultraviolet photons as seen in Fig. 3b. A second reason is that the absorption of blue and ultraviolet photons is competitive between the perovskite, the spiro-OMeTAD and the rutile TNR ETL, all three of which have high absorption coefficients in this spectra range. Previous reports have shown that photons absorbed by the spiro-OMeTAD layer are not efficiently harvested and mostly lost to recombination [52]. Furthermore, while electron hole pairs generated in the perovskite are well-separated through electron transfer to the TiO_2 and hole transfer to spiro-OMeTAD following hole diffusion in the perovskite layer, it is unclear if photogenerated holes in TiO_2 are able to efficiently transfer into the perovskite layer. The high optical path lengths due to scattering within the ETL and active layer of HPSCs based on C-type

TNRs, for photons with 500-600 nm wavelengths (Fig. 3a), enables improved quantum yields in this spectral range as seen in Fig. 4c. It is clear in the IPCE spectra in Fig. 4 (c) that HPSCs fabricated using B-type long TNRs exhibit superior external quantum yields over the entire spectral range compared to HPSCs fabricated using other TNR morphologies.

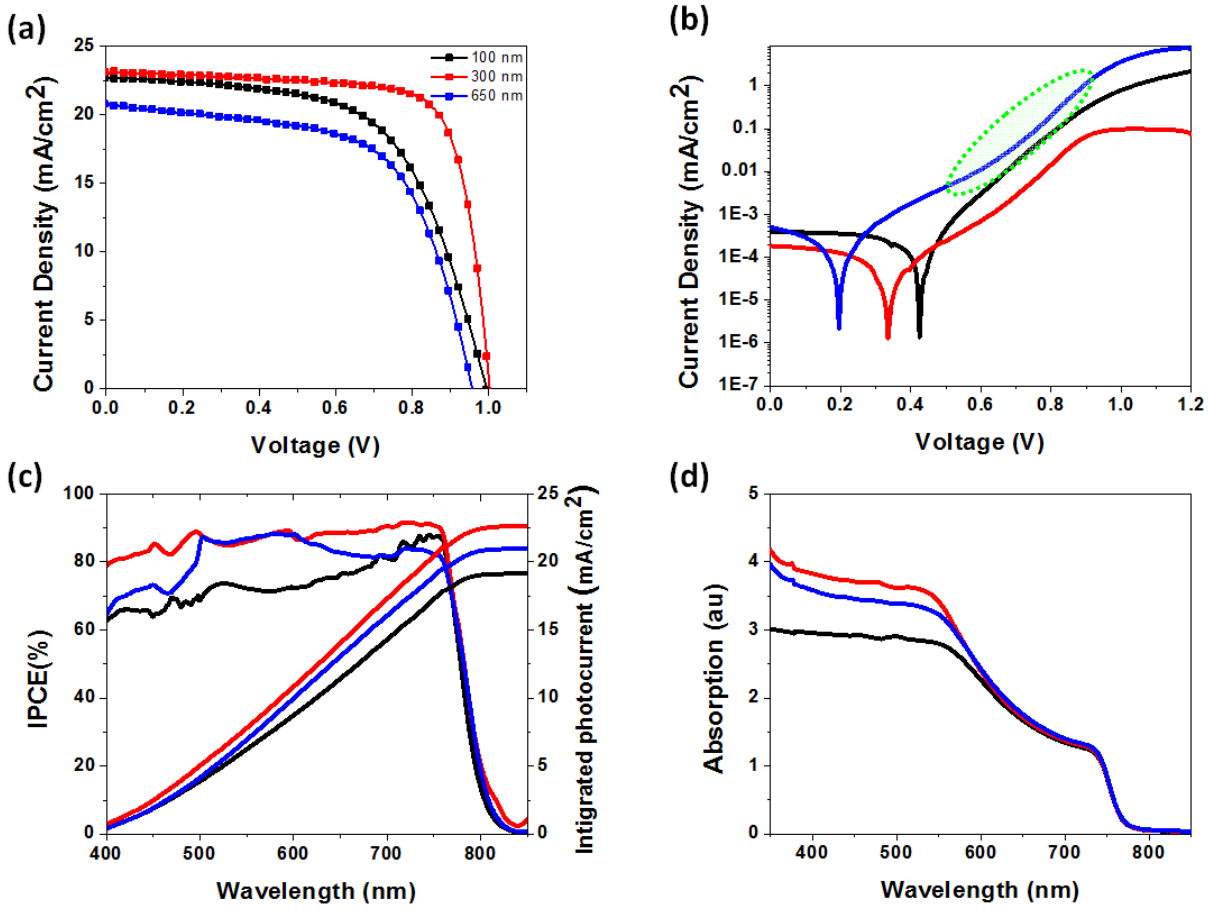

Fig. 4. (a) Current-voltage characteristics under AM 1.5 one sun illumination (b) Dark current-voltage characteristics plotted on a semi-log scale (c) Action spectra showing the external quantum yields of perovskite solar cells with different TNRs (d) UV-vis of perovskite layer over different TNRs. Black, red, and blue color represent A-type, B-type and C-type morphologies titania nanorods respectively.

Fig. 4(b) compares the dark *J-V* characteristics of devices with different types of nanorods. Solar cells based on B-type TNRs (red curve in Fig. 4b) exhibit the smallest dark current in the reverse bias region followed by solar cells based on A-type and C-type TNRs

(black curve and blue curve respectively in Fig. 4b). This indicates a higher shunt resistance and consequently a better fill factor for solar cells based on B-type nanorods. It is apparent that decreasing the length of the nanorods, increased the onset of the dark current; this implies better suppression of charge recombination in devices with smaller nanorods. It is therefore not a coincidence that the solar cells exhibiting the smallest dark current (red curve in Fig. 4b) also result in the highest efficiency (see Fig. 4a). In the forward bias region, solar cells based on B-type and C-type nanorods exhibit the clear signature of space charge limited currents with the green oval in Fig. 4b highlighting the several orders of magnitude increase in the dark current for C-type nanorods when the majority carriers (electrons) injected from the contact electrodes exceed the concentration of deep traps in the nanorods (the trap-free limit), a phenomenon well-explained by us in prior reports [53, 54]. The lowering of the equilibrium carrier concentration in the nanowires due to a high density of deep level surface traps paradoxically enables the achievement of high efficiencies by suppressing the process of back electron transfer i.e. the recombination of electrons in the ETL with photogenerated holes in the perovskite at the TiO_2-perovskite interface. Such a deep trap-mediated suppression of interfacial recombination is maximized for a certain morphology, namely B-type nanorods ~ 300 nm long and ~ 40 nm wide, as deduced from the electrical characteristics in Fig. 4. For ~ 20 nm wide A-type nanorods, the concentration of the local electric field at the needle-like NRs seen in Fig. 2b produces a higher dark current due to field emission. For C-type nanorods that are ~ 80 nm wide, interfacial recombination is insufficiently suppressed due to the low surface-to-volume ratio of these NRs as seen in Fig. 2f and the concomitant smaller number of deep level surface traps.

As can be seen in Table 1 and Fig. S2, the open circuit voltage and fill factor of solar cells fabricated using C-type and D-type TNRs were significantly lower than those fabricated

using A-type and B-type TNRs. Apart from the work functions of the electron- and hole-transporting layers, the interfacial recombination rate plays a crucial role in determining the V_{oc} value [55-57]. Thus, to have a better understanding on the effect of nanorod morphology on recombination at the TNR/perovskite interface, we performed solid state impedance spectroscopy in the dark at a forward bias of 1 V [57-61].

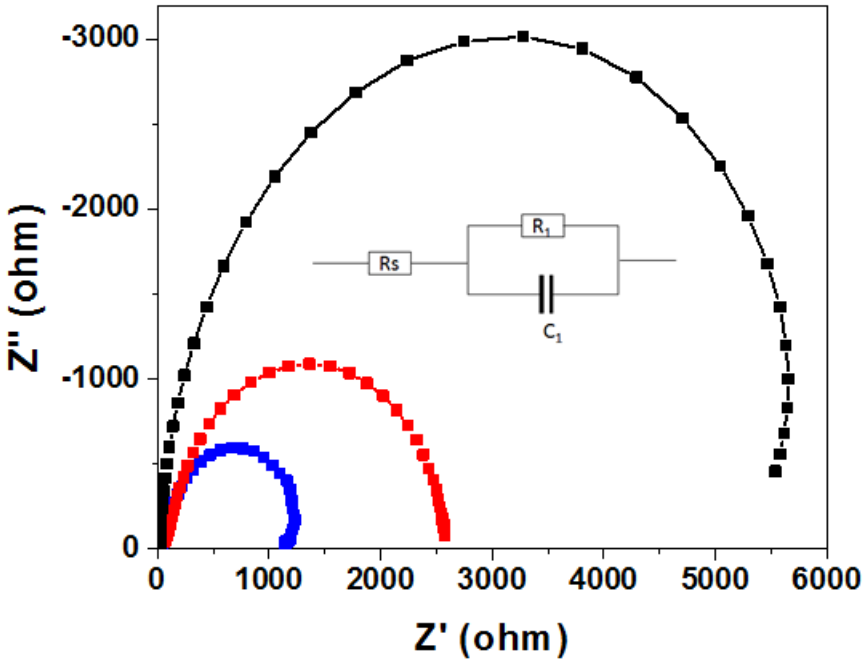

Fig. 5. Nyquist impedance plot of solar cells with different types of nanorods, in the frequency range 1 MHz - 1 Hz at a forward bias of 1 V. Black, red, and blue color represent A-type, B-type and C-type TiO_2 nanorods respectively.

Nyquist plots shown in Fig. 5 were dominated by the large semicircle for the low frequency region while no arc for high frequency region related to perovskite/Spiro-OMeTAD was observed. An arc related to related to the perovskite/HTL interface is typically only observed if the TiO_2 ETL thickness is 2-3 µm thick or higher [61]. Detailed analysis to calculate recombination resistance was performed by extracting the equivalent circuit shown in the inset of Fig. 5. R_s represents the series resistance attributed to the connecting wires and FTO substrate. R_1

and C_1 represent the resistance and capacitance at the interface between TiO_2 nanorod and perovskite active layer respectively. Recombination at the TiO_2/perovskite interface is inversely proportional to the recombination resistance (R_1). A higher value of R_1 implies a lower recombination rate at the interface, which in turn correlates to higher value of V_{oc} and a higher FF. In Fig. 5, the diameter of the arc corresponding to solar cells based on A-type TNRs is longest followed by that of solar cell based on B-type and C-type TNRs respectively. The recombination resistance decreased with increment in the length of the nanorods which corresponds to the expected higher recombination rate for longer nanorods, due to the longer interaction times of electrons transiting through the nanorods with holes in the perovskite, resulting in a lower open circuit voltage and fill factor for the solar cells based on longer nanorods. To compare the photovoltaic performance of TiO_2 nanorod with mesoporous TiO_2 and compact TiO_2 we prepared perovskite solar cells using compact TiO_2 and mesoporous TiO_2 as ETL while other fabrication conditions keeping unchanged. Figs. S3, S4 and S5 show cross-sectional images of TiO_2 nanorod, mesoporous-based, and planar type devices respectively. Devices using a compact TiO_2 layer as ETL showed an inferior PCE of 7.46% with J_{sc}, V_{oc} and FF of 15.40 $mAcm^{-2}$, 0.91 V and 0.53 respectively. Devices using mesoporous TiO_2 were found to have a PCE of about 11.23 % with V_{oc}, J_{sc} and FF of 0.99 V, 19.47 $mAcm^{-2}$ and 0.58 respectively. The current-voltage characteristic of devices with different TiO_2 under layers under AM 1.5 G solar irradiance is depicted in Fig. 6a. The trend of short circuit density obtained using different types of TiO_2 layer is in good agreement in the IPCEs in Fig. 6b. The IPCE values of devices with TNRs are superior to devices with mesoporous TiO_2 and compact TiO_2 because of enhanced charge separation and charge carrier collection efficiencies.

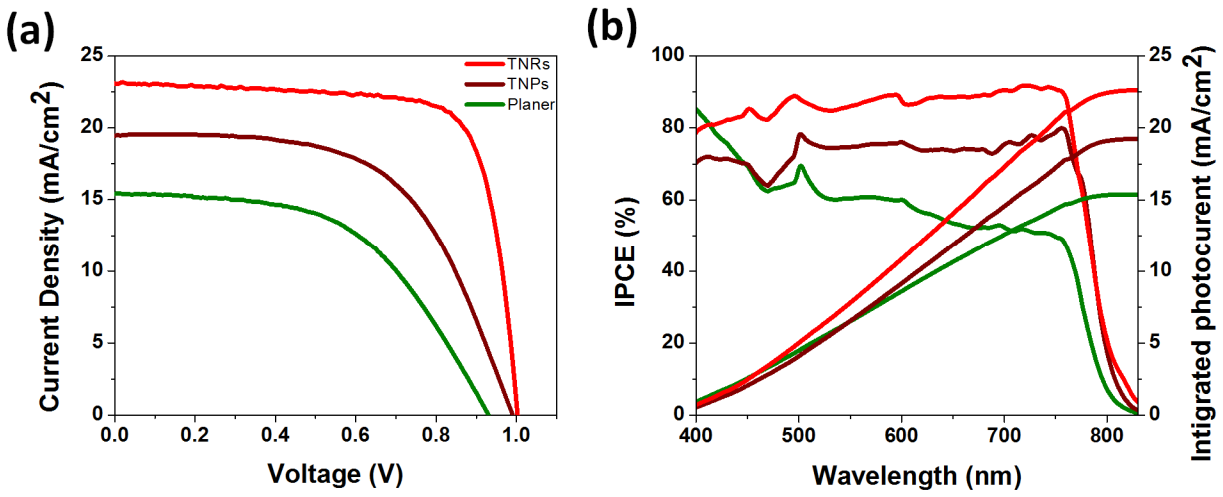

Fig. 6. (a) Current-voltage characteristics (b) IPCE spectra of perovskite solar cell with different TiO_2 underlayer. Red, wine and olive colored lines represents corresponding curves for TiO_2 nanorods, mesoporous TiO_2 and planar TiO_2 respectively.

To further study the charge transfer properties of different TiO_2 ETLs in HPSCs, steady state photoluminescence measurements were performed. As shown in Fig. 7a, TiO_2 nanorods perform a stronger quenching of the perovskite photoluminescence (PL) compared to mesoporous TiO_2 and compact TiO_2. The same trend is observed in the time-resolved PL data obtained though two-photon fluorescence lifetime imaging microscopy (FLIM), as shown in Fig. 7b. The use of two photon excitation enables uniform optical excitation of the entire thickness of the perovskite layer, which is particularly important considering the high absorption coefficient of halide perovskites for supra-bandgap illumination. The PL lifetimes for compact TiO_2, mesoporous TiO_2 and TNRs were found to be 0.87 ns, 0.49 ns and 0.17 ns respectively, which is indicative of photogenerated electron-hole pairs being well-separated in solar cells based on TNRs (through electron injection into TiO_2) before geminate recombination. Taken together, the steady-state and time-resolved PL spectra point to superior charge separation at the TiO_2 nanorod-perovskite

interface compared to the interfaces of perovskite with mesoporous TiO_2 and compact TiO_2 films, which likely also explains the superior photovoltaic performance of solar cells based on TiO_2 nanorod arrays, particularly with regards to the J_{sc} values obtained (Fig. 6).

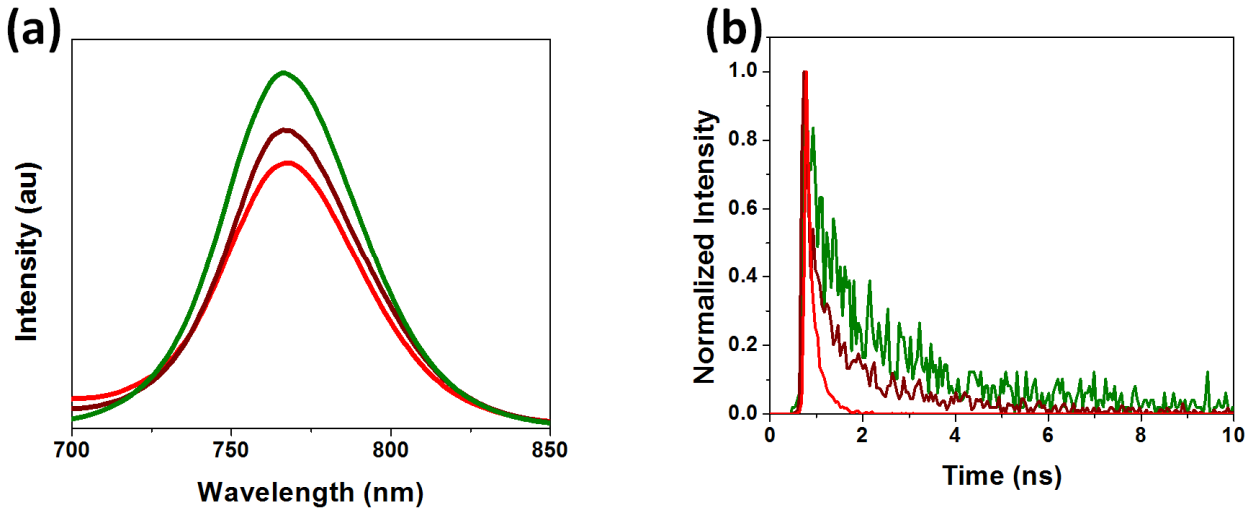

Fig. 7. (a) Steady state photoluminescence spectrum and (b) FLIM spectra of perovskite on different TiO_2 electron transporting underlayers. Red, wine and olive colored lines represents corresponding curves for TNR, mesoporous TiO_2 and planar TiO_2 respectively.

4. Conclusion

In summary, changing the size of the nanorods by varying the concentration of the titanium source in the hydrothermal precursor solution was found to have dramatic effects on the photovoltaic performance of halide perovskite solar cells that used monocrystalline rutile nanorod arrays as the electron transport layer. B-type titania nanorod arrays with a width of ~ 40 nm and a length of ~ 300 nm outperformed other nanorod morphologies as well as mesoporous TiO_2 and planar TiO_2 ETLs in perovskite solar cells with a champion device efficiency of 17.6 %. The superior performance of B-type TNRs was due to optimal light harvesting, excellent charge separation and low interfacial recombination.

Author Contributions: U.K.T. planned and performed the experiments, and collected *J-V*, IPCE, SSIS and PL data and wrote the first draft of the manuscript. A.M.A. assisted in device fabrication and testing. R.K. collected FESEM images, B.D.W. collected UV-Vis data, P.K. collected and analyzed FLIM data, and also modeled the SSIS data. K.S. provided guidance in characterization and data analysis, and edited the manuscript.

Conflicts of Interest: The authors declare no conflict of interest.

Acknowledgements: All authors thank NSERC, CMC Microsystems and NRC-NINT for direct and indirect (equipment) funding support. The infrastructure for solar cell fabrication and testing was made available through a LOF grant to K.S. from the Canada Foundation for Innovation (CFI) matched by the Alberta Small Equipment Grants Program (SEGP). A.M.A. and B.D.W. acknowledge scholarship funding from Alberta Innovates Technology Futures. P. K. thanks Dr. Xuejun Sun at the Cell Imaging Facility for assistance with FLIM.

References

[1] A. Kojima, K. Teshima, Y. Shirai, T. Miyasaka, Novel Photoelectrochemical Cell with Mesoscopic Electrodes Sensitized by Lead-halide Compounds (5), Meeting Abstracts MA2007-02 (2007) 352.
[2] A. Kojima, K. Teshima, Y. Shirai, T. Miyasaka, Organometal Halide Perovskites as Visible-Light Sensitizers for Photovoltaic Cells, J. Am. Chem. Soc. 131 (2009) 6050-6051.
[3] M.A. Green, K. Emery, Y. Hishikawa, W. Warta, E.D. Dunlop, D.H. Levi, A.W.Y. Ho-Baillie, Solar cell efficiency tables (version 49), Progress in Photovoltaics: Research and Applications 25 (2017) 3-13.
[4] E. Edri, S. Kirmayer, A. Henning, S. Mukhopadhyay, K. Gartsman, Y. Rosenwaks, G. Hodes, D. Cahen, Why Lead Methylammonium Tri-Iodide Perovskite-Based Solar Cells Require a Mesoporous Electron Transporting Scaffold (but Not Necessarily a Hole Conductor), Nano Lett. 14 (2014) 1000-1004.
[5] G.E. Eperon, S.D. Stranks, C. Menelaou, M.B. Johnston, L.M. Herz, H.J. Snaith, Formamidinium lead trihalide: a broadly tunable perovskite for efficient planar heterojunction solar cells, Energ. Environ. Sci. 7 (2014) 982-988.
[6] G. Xing, N. Mathews, S. Sun, S.S. Lim, Y.M. Lam, M. Graetzel, S. Mhaisalkar, T.C. Sum, Long-Range Balanced Electron- and Hole-Transport Lengths in Organic-Inorganic CH3NH3PbI3, Science 342 (2013) 344-347.
[7] S.D. Stranks, G.E. Eperon, G. Grancini, C. Menelaou, M.J.P. Alcocer, T. Leijtens, L.M. Herz, A. Petrozza, H.J. Snaith, Electron-Hole Diffusion Lengths Exceeding 1 Micrometer in an Organometal Trihalide Perovskite Absorber, Science 342 (2013) 341-344.
[8] A. Polman, H.A. Atwater, Photonic design principles for ultrahigh-efficiency photovoltaics, Nat. Mater. 11 (2012) 174-177.

[9] Y. Cui, D. van Dam, S.A. Mann, N.J.J. van Hoof, P.J. van Veldhoven, E.C. Garnett, E.P.A.M. Bakkers, J.E.M. Haverkort, Boosting Solar Cell Photovoltage via Nanophotonic Engineering, Nano Lett. 16 (2016) 6467-6471.
[10] J. Lin, K. Liu, X.F. Chen, Synthesis of Periodically Structured Titania Nanotube Films and Their Potential for Photonic Applications, Small 7 (2011) 1784-1789.
[11] C.T. Yip, H.T. Huang, L.M. Zhou, K.Y. Xie, Y. Wang, T.H. Feng, J.S. Li, W.Y. Tam, Direct and Seamless Coupling of TiO2 Nanotube Photonic Crystal to Dye-Sensitized Solar Cell: A Single-Step Approach, Adv. Mater. 23 (2011) 5624-+.
[12] M. Guo, K.Y. Xie, J. Lin, Z.H. Yong, C.T. Yip, L.M. Zhou, Y. Wang, H.T. Huang, Design and coupling of multifunctional TiO2 nanotube photonic crystal to nanocrystalline titania layer as semi-transparent photoanode for dye-sensitized solar cell, Energ. Environ. Sci. 5 (2012) 9881-9888.
[13] X. Zhang, F. Han, B. Shi, S. Farsinezhad, G.P. Dechaine, K. Shankar, Photocatalytic Conversion of Diluted CO2 into Light Hydrocarbons Using Periodically Modulated Multiwalled Nanotube Arrays, Angew. Chem., Int. Ed. (2012) n/a-n/a.
[14] O.L. Muskens, S.L. Diedenhofen, B.C. Kaas, R.E. Algra, E.P.A.M. Bakkers, J. Gómez Rivas, A. Lagendijk, Large Photonic Strength of Highly Tunable Resonant Nanowire Materials, Nano Lett. 9 (2009) 930-934.
[15] R. Boppella, A. Mohammadpour, S. Illa, S. Farsinezhad, P. Basak, K. Shankar, S.V. Manorama, Hierarchical rutile TiO 2 aggregates: A high photonic strength material for optical and optoelectronic devices, Acta Mater. 119 (2016) 92-103.
[16] J. Grandidier, D.M. Callahan, J.N. Munday, H.A. Atwater, Light Absorption Enhancement in Thin-Film Solar Cells Using Whispering Gallery Modes in Dielectric Nanospheres, Adv. Mater. 23 (2011) 1272-1276.
[17] A. Mohammadpour, P.R. Waghmare, S.K. Mitra, K. Shankar, Anodic Growth of Large-Diameter Multipodal TiO2 Nanotubes, ACS Nano 4 (2010) 7421-7430.
[18] D. Liu, T.L. Kelly, Perovskite solar cells with a planar heterojunction structure prepared using room-temperature solution processing techniques, Nat. Photonics 8 (2014) 133-138.
[19] E.J. Yeom, S.S. Shin, W.S. Yang, S.J. Lee, W. Yin, D. Kim, J.H. Noh, T.K. Ahn, S.I. Seok, Controllable synthesis of single crystalline Sn-based oxides and their application in perovskite solar cells, J. Mater. Chem. A 5 (2017) 79-86.
[20] W. Ke, G. Fang, Q. Liu, L. Xiong, P. Qin, H. Tao, J. Wang, H. Lei, B. Li, J. Wan, G. Yang, Y. Yan, Low-Temperature Solution-Processed Tin Oxide as an Alternative Electron Transporting Layer for Efficient Perovskite Solar Cells, J. Am. Chem. Soc. 137 (2015) 6730-6733.
[21] S.S. Bhande, R.B. Ambade, D.V. Shinde, S.B. Ambade, S.A. Patil, M. Naushad, R.S. Mane, Z.A. Alothman, S.-H. Lee, S.-H. Han, Improved Photoelectrochemical Cell Performance of Tin Oxide with Functionalized Multiwalled Carbon Nanotubes–Cadmium Selenide Sensitizer, ACS Appl. Mater. Interfaces 7 (2015) 25094-25104.
[22] Q. Jiang, L. Zhang, H. Wang, X. Yang, J. Meng, H. Liu, Z. Yin, J. Wu, X. Zhang, J. You, Enhanced electron extraction using SnO2 for high-efficiency planar-structure HC(NH2)2PbI3-based perovskite solar cells, Nature Energy 2 (2016) 16177.
[23] J. Nelson, Continuous-time random-walk model of electron transport in nanocrystalline ${\mathrm{TiO}}_{2}$ electrodes, Phys. Rev. B 59 (1999) 15374-15380.
[24] J. van de Lagemaat, A.J. Frank, Nonthermalized Electron Transport in Dye-Sensitized Nanocrystalline TiO2 Films: Transient Photocurrent and Random-Walk Modeling Studies, The Journal of Physical Chemistry B 105 (2001) 11194-11205.
[25] X. Feng, K. Zhu, A.J. Frank, C.A. Grimes, T.E. Mallouk, Rapid Charge Transport in Dye-Sensitized Solar Cells Made from Vertically Aligned Single-Crystal Rutile TiO2 Nanowires, Angew. Chem., Int. Ed. 51 (2012) 2727-2730.

[26] M. Law, L.E. Greene, J.C. Johnson, R. Saykally, P. Yang, Nanowire dye-sensitized solar cells, Nat. Mater. 4 (2005) 455-459.
[27] H.-S. Kim, J.-W. Lee, N. Yantara, P.P. Boix, S.A. Kulkarni, S. Mhaisalkar, M. Grätzel, N.-G. Park, High Efficiency Solid-State Sensitized Solar Cell-Based on Submicrometer Rutile TiO2 Nanorod and CH3NH3PbI3 Perovskite Sensitizer, Nano Lett. 13 (2013) 2412-2417.
[28] K. Mahmood, B.S. Swain, A.R. Kirmani, A. Amassian, Highly efficient perovskite solar cells based on a nanostructured WO3-TiO2 core-shell electron transporting material, J. Mater. Chem. A 3 (2015) 9051-9057.
[29] Z. Gu, F. Chen, X. Zhang, Y. Liu, C. Fan, G. Wu, H. Li, H. Chen, Novel planar heterostructure perovskite solar cells with CdS nanorods array as electron transport layer, Sol. Energy Mater. Sol. Cells 140 (2015) 396-404.
[30] X. Li, S.-M. Dai, P. Zhu, L.-L. Deng, S.-Y. Xie, Q. Cui, H. Chen, N. Wang, H. Lin, Efficient Perovskite Solar Cells Depending on TiO2 Nanorod Arrays, ACS Appl. Mater. Interfaces 8 (2016) 21358-21365.
[31] K. Mahmood, B.S. Swain, A. Amassian, 16.1% Efficient Hysteresis-Free Mesostructured Perovskite Solar Cells Based on Synergistically Improved ZnO Nanorod Arrays, Advanced Energy Materials 5 (2015) 1500568-n/a.
[32] J. Qiu, Y. Qiu, K. Yan, M. Zhong, C. Mu, H. Yan, S. Yang, All-solid-state hybrid solar cells based on a new organometal halide perovskite sensitizer and one-dimensional TiO2 nanowire arrays, Nanoscale 5 (2013) 3245-3248.
[33] Q. Jiang, X. Sheng, Y. Li, X. Feng, T. Xu, Rutile TiO2 nanowire-based perovskite solar cells, Chem. Commun. 50 (2014) 14720-14723.
[34] B.C. O'Regan, J.R. Durrant, P.M. Sommeling, N.J. Bakker, Influence of the TiCl4 Treatment on Nanocrystalline TiO2 Films in Dye-Sensitized Solar Cells. 2. Charge Density, Band Edge Shifts, and Quantification of Recombination Losses at Short Circuit, J. Phys. Chem. C 111 (2007) 14001-14010.
[35] J. Bandara, K. Shankar, J. Basham, H. Wietasch, M. Paulose, O.K. Varghese, C.A. Grimes, M. Thelakkat, Integration of TiO2 nanotube arrays into solid-state dye-sensitized solar cells, Eur. Phys. J. Appl. Phys. 53 (2011) 20601.
[36] T.-H. Meen, Y.-T. Jhuo, S.-M. Chao, N.-Y. Lin, L.-W. Ji, J.-K. Tsai, T.-C. Wu, W.-R. Chen, W. Water, C.-J. Huang, Effect of TiO2 nanotubes with TiCl4 treatment on the photoelectrode of dye-sensitized solar cells, Nanoscale Research Letters 7 (2012) 579.
[37] W. Shockley, H.J. Queisser, Detailed Balance Limit of Efficiency of p-n Junction Solar Cells, J. Appl. Phys. 32 (1961) 510-519.
[38] B. Yang, O. Dyck, J. Poplawsky, J. Keum, A. Puretzky, S. Das, I. Ivanov, C. Rouleau, G. Duscher, D. Geohegan, K. Xiao, Perovskite Solar Cells with Near 100% Internal Quantum Efficiency Based on Large Single Crystalline Grains and Vertical Bulk Heterojunctions, J. Am. Chem. Soc. 137 (2015) 9210-9213.
[39] J.M. Ball, M.M. Lee, A. Hey, H.J. Snaith, Low-temperature processed meso-superstructured to thin-film perovskite solar cells, Energ. Environ. Sci. 6 (2013) 1739-1743.
[40] D.K. Chaudhary, P. Kumar, L. Kumar, Evolution in surface coverage of CH 3 NH 3 PbI 3− X Cl X via heat assisted solvent vapour treatment and their effects on photovoltaic performance of devices, RSC Adv. 6 (2016) 94731-94738.
[41] H. Liu, Z. Huang, S. Wei, L. Zheng, L. Xiao, Q. Gong, Nano-structured electron transporting materials for perovskite solar cells, Nanoscale 8 (2016) 6209-6221.
[42] N. Tétreault, M. Grätzel, Novel nanostructures for next generation dye-sensitized solar cells, Energ. Environ. Sci. 5 (2012) 8506-8516.
[43] A. Fakharuddin, F. Di Giacomo, I. Ahmed, Q. Wali, T.M. Brown, R. Jose, Role of morphology and crystallinity of nanorod and planar electron transport layers on the performance and long term durability of perovskite solar cells, J. Power Sources 283 (2015) 61-67.

[44] Y. Cui, X. He, M. Zhu, X. Li, Preparation of anatase TiO2 microspheres with high exposure (001) facets as the light-scattering layer for improving performance of dye-sensitized solar cells, J. Alloys Compd. 694 (2017) 568-573.
[45] H. Yu, J. Pan, Y. Bai, X. Zong, X. Li, L. Wang, Hydrothermal Synthesis of a Crystalline Rutile TiO2 Nanorod Based Network for Efficient Dye-Sensitized Solar Cells, Chemistry-A European Journal 19 (2013) 13569-13574.
[46] S. Hore, C. Vetter, R. Kern, H. Smit, A. Hinsch, Influence of scattering layers on efficiency of dye-sensitized solar cells, Sol. Energy Mater. Sol. Cells 90 (2006) 1176-1188.
[47] H. Zhang, H. Yu, Y. Han, P. Liu, S. Zhang, P. Wang, Y. Cheng, H. Zhao, Rutile TiO2 microspheres with exposed nano-acicular single crystals for dye-sensitized solar cells, Nano Res. 4 (2011) 938-947.
[48] J.-D. Peng, C.-P. Lee, D. Velayutham, V. Suryanarayanan, K.-C. Ho, Dye-sensitized solar cells containing mesoporous TiO2 spheres as photoanodes and methyl sulfate anion based biionic liquid electrolytes, J. Mater. Chem. A 3 (2015) 6383-6391.
[49] J. Huo, Y. Hu, H. Jiang, W. Huang, C. Li, SnO2 nanorod@TiO2 hybrid material for dye-sensitized solar cells, J. Mater. Chem. A 2 (2014) 8266-8272.
[50] O.K. Varghese, M. Paulose, C.A. Grimes, Long vertically aligned titania nanotubes on transparent conducting oxide for highly efficient solar cells, Nat Nano 4 (2009) 592-597.
[51] P. Löper, M. Stuckelberger, B. Niesen, J. Werner, M. Filipič, S.-J. Moon, J.-H. Yum, M. Topič, S. De Wolf, C. Ballif, Complex Refractive Index Spectra of CH3NH3PbI3 Perovskite Thin Films Determined by Spectroscopic Ellipsometry and Spectrophotometry, The Journal of Physical Chemistry Letters 6 (2015) 66-71.
[52] X. Wang, Z. Li, W. Xu, S.A. Kulkarni, S.K. Batabyal, S. Zhang, A. Cao, L.H. Wong, TiO2 nanotube arrays based flexible perovskite solar cells with transparent carbon nanotube electrode, Nano Energy 11 (2015) 728-735.
[53] A. Mohammadpour, S. Farsinezhad, B.D. Wiltshire, K. Shankar, Majority carrier transport in single crystal rutile nanowire arrays, physica status solidi (RRL) – Rapid Research Letters (2014) n/a-n/a.
[54] A. Mohammadpour, B.D. Wiltshire, Y. Zhang, S. Farsinezhad, A.M. Askar, R. Kisslinger, Y. Ren, P. Kar, K. Shankar, 100-fold improvement in carrier drift mobilities in alkanephosphonate-passivated monocrystalline TiO 2 nanowire arrays, Nanotechnology 28 (2017) 144001.
[55] W. Yan, Y. Li, S. Ye, Y. Li, H. Rao, Z. Liu, S. Wang, Z. Bian, C. Huang, Increasing open circuit voltage by adjusting work function of hole-transporting materials in perovskite solar cells, Nano Res. 9 (2016) 1600-1608.
[56] B. Suarez, V. Gonzalez-Pedro, T.S. Ripolles, R.S. Sanchez, L. Otero, I. Mora-Sero, Recombination study of combined halides (Cl, Br, I) perovskite solar cells, The journal of physical chemistry letters 5 (2014) 1628-1635.
[57] I. Mora-Seró, S. Giménez, F. Fabregat-Santiago, E. Azaceta, R. Tena-Zaera, J. Bisquert, Modeling and characterization of extremely thin absorber (eta) solar cells based on ZnO nanowires, Phys. Chem. Chem. Phys. 13 (2011) 7162-7169.
[58] S.S. Mali, C.S. Shim, H.K. Park, J. Heo, P.S. Patil, C.K. Hong, Ultrathin Atomic Layer Deposited TiO2 for Surface Passivation of Hydrothermally Grown 1D TiO2 Nanorod Arrays for Efficient Solid-State Perovskite Solar Cells, Chem. Mater. 27 (2015) 1541-1551.
[59] M. Lv, X. Dong, X. Fang, B. Lin, S. Zhang, X. Xu, J. Ding, N. Yuan, Improved photovoltaic performance in perovskite solar cells based on CH3NH3PbI3 films fabricated under controlled relative humidity, RSC Adv. 5 (2015) 93957-93963.
[60] I. Mora-Sero, S. Gimenez, F. Fabregat-Santiago, E. Azaceta, R. Tena-Zaera, J. Bisquert, Modeling and characterization of extremely thin absorber (eta) solar cells based on ZnO nanowires, Phys. Chem. Chem. Phys. 13 (2011) 7162-7169.

[61] H.-S. Kim, I. Mora-Sero, V. Gonzalez-Pedro, F. Fabregat-Santiago, E.J. Juarez-Perez, N.-G. Park, J. Bisquert, Mechanism of carrier accumulation in perovskite thin-absorber solar cells, Nat. Commun. 4 (2013).

Supporting Information

Impact of morphology of hydrothermally grown TiO_2 nanorods on electron transporting property in perovskite solar cells

Ujwal Kumar Thakur[1], Abdelrahman M. Askar[1], Ryan Kisslinger[1], Benjamin Wiltshire[1,2], Piyush Kar[1], Karthik Shankar[*,1,2]

[1]*Department of Electrical and Computer Engineering, University of Alberta, 9211-116 St, Edmonton, Alberta, T6G 1H9, Canada*

[2]*NRC National Institute for Nanotechnology, 11421 Saskatchewan Dr NW, Edmonton, AB T6G 2M9, Canada*

***Correspondence**
Karthik Shankar, Department of Electrical and Computer Engineering, University of Alberta, 9211-116 St, Edmonton, Alberta, T6G 1H9, Canada

E-mail: kshankar@ualberta.ca

Keywords: Perovskite solar cells, nanostructured electron transporting layer, TiO_2 nanorods

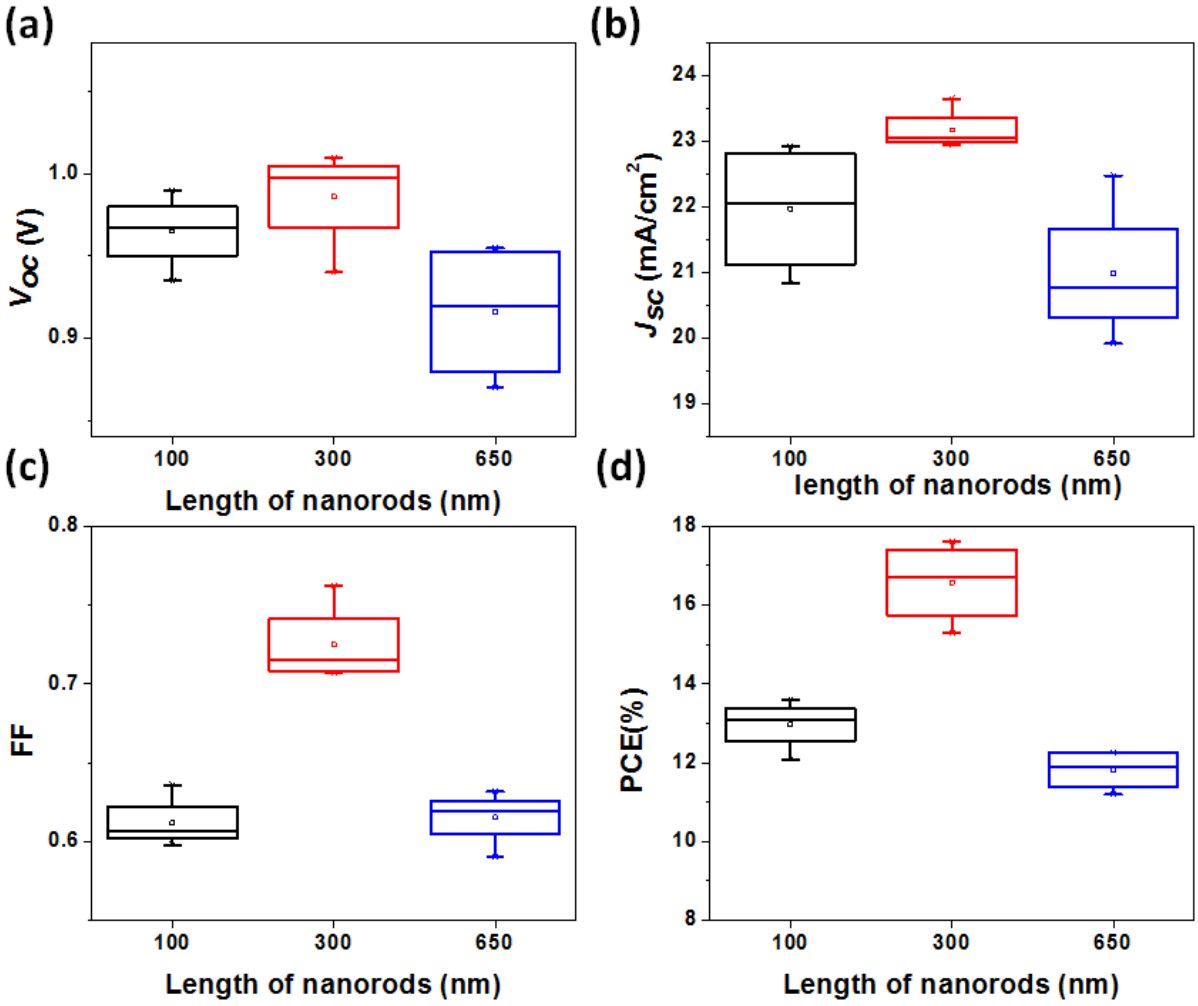

Figure S1. Summary of the performance of halide perovskite solar cells for different nanorod morphologies: (a) V_{oc}, (b) J_{sc}, (c) *FF* and (d) PCE. All the performance data were measured at AM 1.5 G with an intensity of 100 mWcm^{-2}.

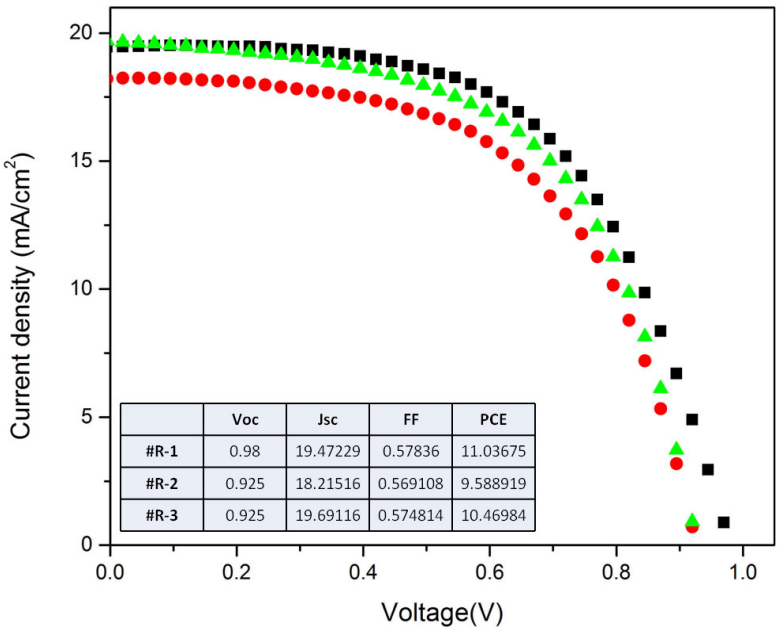

	Voc	Jsc	FF	PCE
#R-1	0.98	19.47229	0.57836	11.03675
#R-2	0.925	18.21516	0.569108	9.588919
#R-3	0.925	19.69116	0.574814	10.46984

Figure S2. J-V curves of halide perovskite solar cells constructed using nanorods ~ 150 nm in width and ~ 1 µm in length, formed using 1000 µl of TBO in the hydrothermal precursor solution. The data were measured at AM 1.5 G with an intensity of 100 mW cm^{-2}.

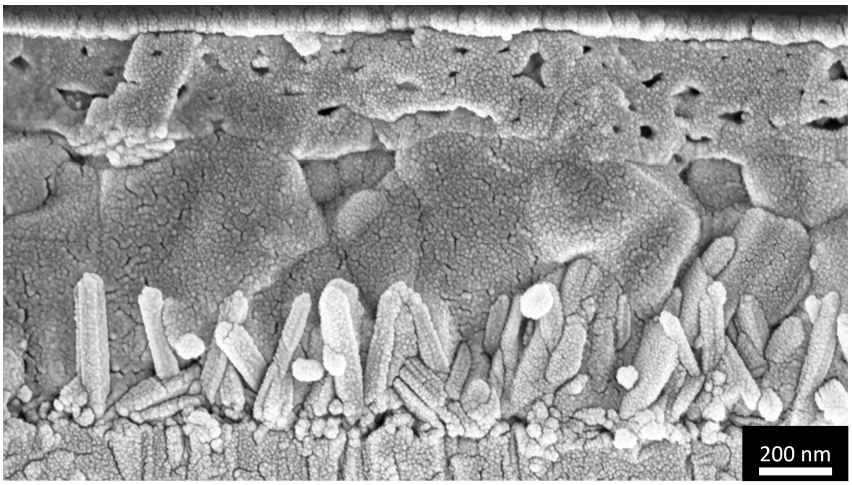

Figure S3: Cross-sectional FESEM image of PSC based on 300 nm long TiO_2 nanorods.

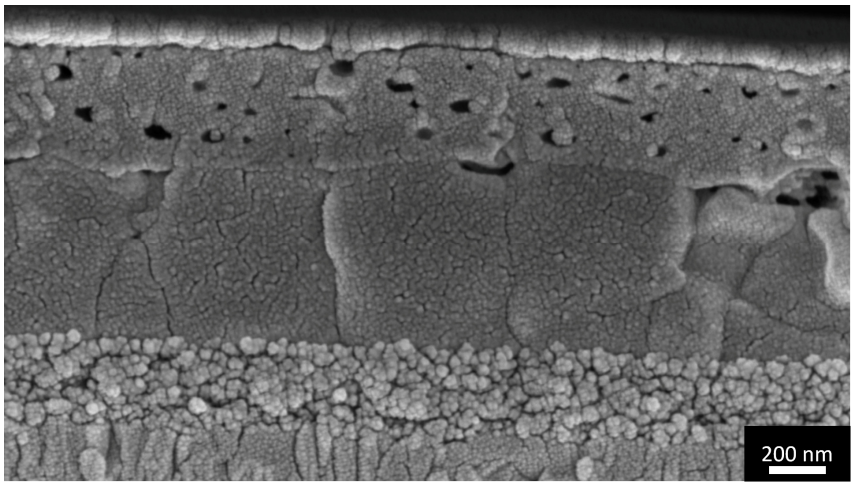

Figure S4: Cross-sectional FESEM image of PSC fabricated over 200 nm of mesoporous TiO_2.

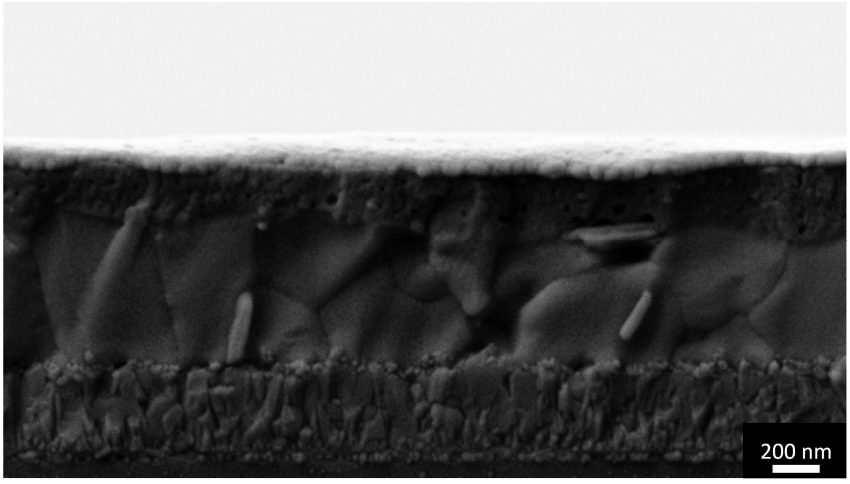

Figure S5: Cross-sectional SEM image of PSC fabricated over compact TiO_2.